Salt crystallisation and weathering in masonry retaining walls

A multiphase modelling approach

Sharma, Satyadhrik; Esposito, Rita; D'Altri, Antonio Maria; Castellazzi, Giovanni

DOI
10.1016/j.jobe.2025.112999

Publication date
2025

Document Version
Final published version

Published in
Journal of Building Engineering

Citation (APA)
Sharma, S., Esposito, R., D'Altri, A. M., & Castellazzi, G. (2025). Salt crystallisation and weathering in masonry retaining walls: A multiphase modelling approach. *Journal of Building Engineering*, *111*, Article 112999. https://doi.org/10.1016/j.jobe.2025.112999

Journal of Building Engineering 111 (2025) 112999

Contents lists available at ScienceDirect

Journal of Building Engineering

journal homepage: www.elsevier.com/locate/jobe

Salt crystallisation and weathering in masonry retaining walls: A multiphase modelling approach

Satyadhrik Sharma [a,*], Rita Esposito [a], Antonio Maria D'Altri [b], Giovanni Castellazzi [b]

[a] Department of Materials, Mechanics, Management & Design, Section of Applied Mechanics, Faculty of Civil Engineering and Geosciences, Delft University of Technology (TU Delft), Delft, the Netherlands
[b] Department of Civil, Chemical, Environmental, and Materials Engineering, University of Bologna, Bologna, Italy

ARTICLE INFO

Keywords:
Masonry degradation
Salt crystallisation
Quay walls
Multi-wythe walls
Porous material

ABSTRACT

This study presents a numerical investigation into the effects of salt crystallisation-induced weathering on masonry earth-retaining walls, with a specific focus on historic quay walls in Amsterdam. A multiphase modelling strategy is adopted to simulate moisture and salt transport, capturing the impact of environmental exposure on these ageing structures. The numerical model is first applied with masonry assumed as a homogeneous continuum and is subsequently refined to incorporate masonry texture. The influence of boundary conditions, multiple weathering cycles, and long-term humidity variations is examined to assess salt accumulation patterns. Results indicate that evaporation pathways significantly influence crystallisation depth, while explicitly modelling masonry texture leads to greater salt accumulation. Furthermore, an analytical estimation of the effective Young's modulus suggests that salt deposition within pores may contribute to through-thickness stiffness variations observed in experimental studies on samples collected from a multi-wythe masonry bridge pillar, with masonry type and exposure conditions comparable to those of Amsterdam's quay walls. These findings provide new insights into the deterioration mechanisms of historic quay walls and highlight the importance of considering environmental effects in their structural assessment.

1. Introduction

Masonry earth-retaining walls are found in numerous countries worldwide [1–8]. Despite having endured long service lives under often hostile environmental conditions, many of these walls remain operational and continue to serve as critical components of urban infrastructure in several cities such as Amsterdam, Venice and Hamburg. However, this ageing stock of structures is now facing accelerated deterioration, largely driven by environmental factors such as temperature and moisture fluctuations, both of which are projected to intensify as a result of climate change [9–12]. Structural assessments of these walls typically neglect the detrimental effects of environmental loads, instead assuming ideal conditions. As a result, the real vulnerability associated with these structures may be underestimated.

The long-term assessment of existing masonry infrastructure [13–21] is therefore essential for ensuring its sustainability, resilience, and durability. A comprehensive understanding of ageing mechanisms is critical to support maintenance strategies and the continued

* Corresponding author.
E-mail address: S.Sharma-9@tudelft.nl (S. Sharma).

https://doi.org/10.1016/j.jobe.2025.112999
Received 3 March 2025; Received in revised form 19 May 2025; Accepted 24 May 2025
Available online 27 May 2025

serviceability of historic masonry infrastructure in the context of changing climatic demands, further underscoring the need to develop and validate more accurate numerical modelling approaches that capture the impact of environmental weathering on masonry earth-retaining walls.

Among the primary degradation risks faced by a porous building material like masonry, salt crystallisation stands out [22]. Although several accelerated experimental test protocols have been lately developed in Refs. [23–27] to estimate the resistance of porous building materials against salt crystallisation-induced ageing, the reproduction of long-term actual weathering conditions in laboratory appears still challenging. To this aim, numerical tools have been developed in recent years to simulate long-term weathering conditions and damage induced by salt crystallisation in porous media in Refs. [28–30]. For instance, a coupled model for heat, moisture, and salt transport in porous building materials was introduced in Ref. [31] and later extended in Refs. [32,33] to include salt phase changes and salt crystallisation. Additionally, a multi-physics model for predicting spalling in brick masonry due to in-pore salt crystallisation was developed in Ref. [34]. Another computational model that couples heat, water, and salt ion transport, salt crystallisation, deformation, and damage in porous materials was presented in Ref. [35]. Furthermore, a multi-phase model analysing moisture and salt transport and predicting stress from salt crystallisation in masonry walls was introduced in Ref. [36] and applied in Refs. [37–39], with extensions to account for salt hydration in Ref. [40]. Finally, a coupled chemo-hydro-mechanics approach based on phase-field modelling for simulating cracking and damage from salt crystallisation in pores was also developed in Ref. [41].

Historic masonry quay walls lining the canals of many European cities, particularly in the Netherlands, offer a compelling case study for investigating the effects of salt-induced deterioration. These centuries-old structures have long been exposed to a continuous combination of harsh weather conditions and salts from canal water. Moreover, as active elements of modern urban centres, these quay walls now experience larger and fundamentally different loads than those for which they were originally designed, like increased traffic loads. Historically conceived as gravity retaining walls for flood protection and to accommodate ships, their present condition and structural capacity remain largely unknown. This issue is especially critical in Amsterdam, where the structural state of over 200 km of historic quays is unknown, as evidenced by documented cases of severe damage [1] and collapse [42]. In response, numerous studies have addressed topics such as their structural reliability [43], timber foundation performance [44–49], remote monitoring of quay and building displacements [50–53], the development of renewal strategies [54], and the formulation of structural assessment methods [55,56].

As part of these same efforts, Li and Esposito [57] carried out an experimental characterisation of Amsterdam's historical masonry infrastructure. Although their samples were extracted from a multi-wythe masonry bridge pillar, the exposure conditions and masonry type are considered comparable to those of quay walls, given their similar locations and the likelihood that they were constructed around the same period. Their extensive experimental campaign included, among other, determining the Young's modulus through uniaxial compression tests on T-shaped cores and masonry prisms, with varying height-to-length ratios. In all cases, a "through--thickness effect" was observed, whereby specimens taken from the external side of the pillar, exposed to canal water, exhibited a higher Young's modulus than those from the internal side, with an increase ranging from 30 % to 100 %. This observation partly motivated the present work, as it raises the question of whether environmental effects, particularly salt crystallisation within masonry pores, can significantly alter the effective Young's modulus of historical masonry structures.

To investigate this, a multiphase modelling strategy for the simulation of moisture transport and salt crystallisation in masonry structures [36] is used to estimate the effects of salt crystallisation on multi-wythe masonry quay walls in Amsterdam. The background of the adopted modelling strategy is presented in Section 2. While this approach has been validated against laboratory investigations in the past, this study represents its first application to a real case, where several unknowns must be considered. The numerical model of the case study, namely a historic quay wall in Amsterdam, and an investigation into the effects of some of these unknowns, including boundary conditions, masonry texture, and multiple weathering cycles, are presented in Section 3. The results from this section, in combination with analytical methods, are then used to evaluate whether salt crystallisation could indeed be a contributing factor to the "through-thickness" increase in Young's modulus observed in laboratory investigations by Li and Esposito [57], are discussed in Section 4. Finally, concluding remarks are provided in Section 5.

2. Multiphase modelling strategy

The simulation of moisture and salt transport, and salt crystallisation within masonry earth-retaining walls is here undertaken by means of the multiphase modelling strategy developed in Ref. [36]. Accordingly, a multiphase continuous porous medium composed of the solid matrix, gaseous and liquid water, and liquid and solid salt is conceived. Particularly, sodium chloride, which has a unique solid phase, is here considered, together with the hypothesis of isothermal conditions. The multiphase model is formulated by means of three independent variables, i.e., the mass fraction of the dissolved salt ω, the concentration of crystallised salt c_s^s, and ratio between the actual vapor pressure and the vapor pressure at saturation h (pore relative humidity). The model is then ruled by a (i) moisture mass conservation equation,

$$\frac{\partial c_w}{\partial t} + \nabla \cdot \mathbf{j}_w = 0 \tag{1}$$

being c_w the concentration of moisture, $\mathbf{j}_w$ the water flux ($\mathbf{j}_w = \mathbf{j}_w^g + \mathbf{j}_w^l$, where $\mathbf{j}_w^g$ is the water vapor flux and $\mathbf{j}_w^l$ the water liquid flux), and $\frac{\partial}{\partial t}$ the time derivative, (ii) a salt mass conservation equation,

$$\frac{\partial c_s^l}{\partial t} + \nabla \cdot \mathbf{j}_s^l + \frac{\partial c_s^s}{\partial t} = 0 \tag{2}$$

being c_s^l the concentration of dissolved salt and $\mathbf{j}_s^l$ the flux of dissolved salt, where $\mathbf{j}_w^l$ and $\mathbf{j}_s^l$ can be expressed as $\mathbf{j}_w^l = (1-\omega)\mathbf{j}_{ws}^l - \mathbf{j}_{s,diff}^l$ and $\mathbf{j}_s^l = \omega \mathbf{j}_{ws}^l + \mathbf{j}_{s,diff}^l$, being $\mathbf{j}_{ws}^l$ the flux of the liquid phase and $\mathbf{j}_{s,diff}^l$ the diffusive flux of the dissolved salt, and (iii) an evolution equation defining the kinetics of salt precipitation/dissolution, adopting an isotropic distribution of cylindrical pores and cylindrical nuclei of the same pore radius (r_p),

$$\frac{\partial c_s^s}{\partial t} = \pi\, r_p^2\, \rho_s^s \frac{n}{V_{tot}} K_c \left| \frac{\omega}{\omega_{sat}} - 1 \right|^P \tag{5}$$

with ω_{sat} the mass of dissolved salt per unit mass of liquid phase at saturation, where the supersaturation ratio ω / ω_{sat} is assumed to rule the evolution equation, i.e. crystallisation happens when ω/ω_{sat} overtakes a pre-defined threshold (here adopted equal to 1) and dissolution happens when ω/ω_{sat} is lower than one. Moreover, ρ_s^s is the solid salt density (2160 kg/m^3 in this case), K_c is the growth rate coefficient, V_{tot} the pore volume, and P is the order of the crystallisation process (here adopted equal to 1).

The constitutive relationships for flux $\mathbf{j}_w^g$, capillary liquid flux $\mathbf{j}_{ws}^l$ and diffusive flux of dissolved salt $\mathbf{j}_{s,diff}^l$ can be based on vapor permeability K_g, liquid permeability of the salt solution K_l, and salt diffusion coefficient K_s, as detailed in Refs. [36,37,39]. It should be highlighted that K_l can be expressed in terms of the liquid permeability of the pure water, which in turn is function of the capillary water absorption coefficient A_{cap} of the porous medium (as highlighted, e.g., in Ref. [38]).

In addition, the salt solution saturation degree S_{ws}^l is here defined as a function of the relative humidity h by means of the so-called sorption/desorption curve $S_{ws}^l(h)$, which is typically derived experimentally. Finally, the multiphase model is integrated by the boundary conditions, which can have four different forms, i.e.,

$$\begin{aligned} h &= \overline{h} \\ \omega &= \overline{\omega} \\ \boldsymbol{j}_w \cdot \boldsymbol{n} &= \gamma_w (A_w h - h_{env}) \\ \boldsymbol{j}_s^l \cdot \boldsymbol{n} &= 0 \end{aligned} \tag{6}$$

where $\overline{h}$ and $\overline{\omega}$ are the prescribed humidity and salt concentration, respectively, q_w and q_ω the prescribed normal fluxes of moisture and salt, respectively, $\mathbf{n}$ is the outward unit normal to the boundary, h_{env} the prescribed environmental humidity, A_w the water activity, and γ_w the convective humidity coefficient. A Newton-Raphson method-based iterative strategy is employed to solve the system of nonlinear differential equations. Time integration is conducted by means of the backward finite difference method. Quadratic finite elements are employed to discretise the domain.

3. Application of the modelling strategy

The modelling strategy formulated in Section 2 is applied in this section to a masonry earth-retaining structure located in Amsterdam, the Netherlands. Details of this case study are outlined in Section 3.1, with a summary of the numerical model adopted provided in Section 3.2. Unlike controlled laboratory conditions, where factors such as boundary conditions, prescribed humidity levels, and salt concentrations are well-defined, these variables are often unknown and subject to varying degrees of uncertainty in real-world structures. The impact of these uncertainties is explored in Section 3.3 under the influence of a single weathering cycle. Masonry is initially modelled as a homogenous continuum in these investigations and the model is consequently further developed to examine the effects of explicitly modelling masonry texture (Section 3.5) and the influence of multiple weathering cycles (Section 3.6).

3.1. Case study: masonry earth-retaining wall in Amsterdam, the Netherlands

The modelling strategy is applied to a historical masonry earth-retaining structure, specifically a quay wall, in Amsterdam, Netherlands. These earth-retaining structures are crucial in the Dutch context, where a significant portion of the country lies below sea level and faces the risk of flooding [58]. Quay walls serve vital functions in stabilising shorelines, accommodating ships, and protecting urban areas from water ingress. They are integral to the Netherlands' unique urban fabric and water management system, lining the intricate canal network that characterises its landscape.

The geometry of the case study in this paper is based on archival information [59] about the *Marnixkade* quay in Amsterdam and it is representative of many historical quays in Dutch cities. These quays typically feature a masonry gravity retaining wall supported by a timber floor and timber piles, interspersed with timber beams placed between the floor and foundation piles (Fig. 1a). For the *Marnixkade* quay, the clay brick masonry wall is, on average, 0.65 m thick and 1.40 m high, with a capstone placed on top. The capstone generally does not span the entire width of such quay walls. According to original plans and the dimensions used in this study, the timber floor is 0.07 m thick, while the timber beams have a 0.20 × 0.20 m cross-section and are 2.4 m long, resting on tapered piles.

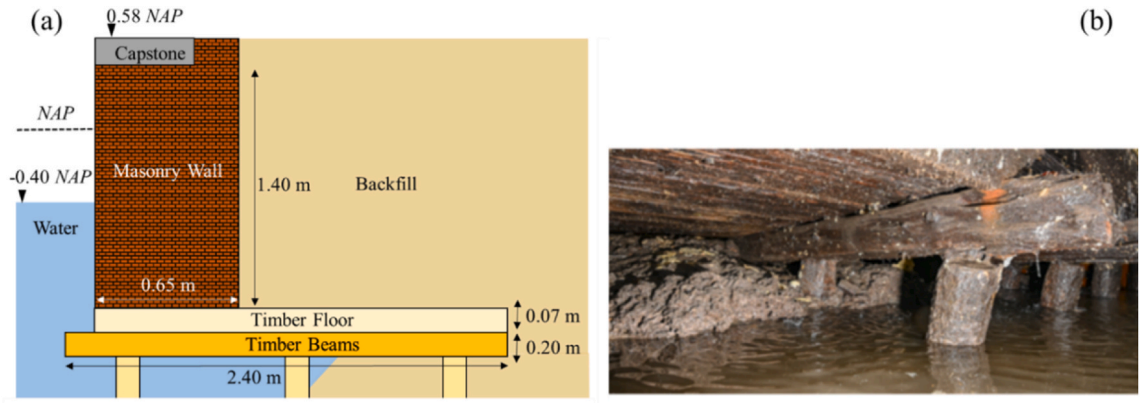

Fig. 1. (a) Geometry of the adopted case-study (transversal cross-section adapted from Refs. [55,56]) and (b) timber floor on top of a timber beam connected to a timber pile (reproduced with permission from Ref. [59]).

The ground level at *Marnixkade* is 0.58 m above *Normaal Amsterdams Peil* (*NAP*), with the water level at −0.40 m *NAP*. *NAP* is the reference plane for water height in the Netherlands, with 0 m NAP approximating the average sea level of the North Sea [60]. Consequently, approximately 0.6 m of the wall is submerged in the canal, leaving the remaining 0.8 m above the water.

3.2. Numerical model of the case study

Based on the information summarised in Section 3.1, a 2D numerical model of the masonry quay wall is constructed (Fig. 2). To facilitate the assignment of boundary conditions, the masonry wall is divided into two blocks: the lower block represents the submerged portion of the wall, while the upper block represents the portion above the waterline. In this model, the masonry is treated as a homogeneous continuum. The adopted mesh is of the mapped type with quadrilateral elements, refined near boundaries where salt crystallisation is expected, such as the canal-facing and backfill-facing wall surface. On top of the wall, an additional block represents the capstone. The model parameters and material properties used in the numerical model are derived from the literature and are

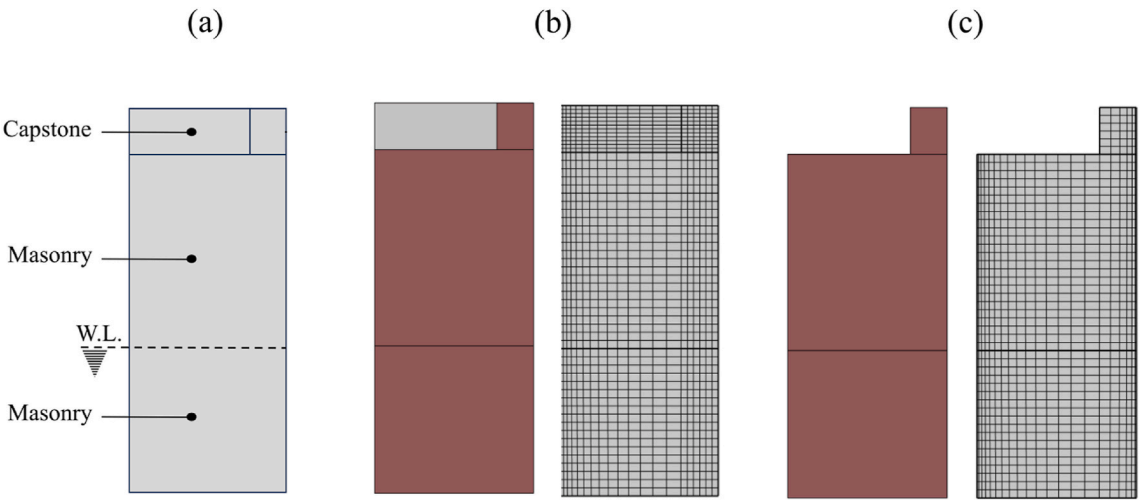

Fig. 2. (a) Schematization of the numerical model and associated mesh; numerical model with the capstone assumed to be composed of (b) a cementitious material, and (c) solid stone.

Table 1
Summary of model parameters and material properties adopted in the numerical model.

Quantity	Masonry	Cementitious Material
Mean pore radius	0.700 μm [4]	0.041 μm [10]
Initial porosity	26.0 % [4]	22.5 % [10]
Water adsorption coefficient A_{cap}	0.185 kg/m^2/s$^{0.5}$ [4]	0.05 kg/m^2/s$^{0.5}$ [10]
Salt diffusion coefficient K_s	0.499 × 10^{-9} m^2/s [4]	0.05 × 10^{-9} m^2/s [2]

detailed in Table 1.

It can be observed in Fig. 2 that the masonry wall is terminated at the position of the timber floor, and its interaction with the surrounding environment is modelled using Dirichlet's and Neumann's type boundary conditions as follows.

- **Wet surfaces**: Dirichlet's type boundary condition is applied to simulate immersion in a saline solution, representing the water of the canals. For the case study under investigation, this applies to the submerged portion of the masonry wall and the section in contact with the timber floor, both of which are assumed to be completely wet in all variations of the numerical model.
- **Evaporative and sealed surfaces**: Neumann's type boundary condition is used to simulate evaporation from the exposed face of the wall above the waterline in all variations of the numerical model. Additionally, variations accounting for evaporation at the wall-capstone and wall-backfill interfaces are also considered. If the capstone is assumed to be made of a cementitious material, it is explicitly modelled, and evaporation is permitted at its exterior face. Conversely, if the capstone is assumed to be made of solid granite, it is not explicitly modelled, and a sealed surface is applied at the wall-capstone interface to prevent evaporation. Similarly, variations are considered for the wall-backfill interface, with evaporation either enabled or disabled depending on the material properties. The variations of the numerical model resulting because of these assumptions are explained in more detail in Section 3.3.

For all simulations reported in this paper, a salt concentration of 0.04 kg/l in the canal water and a relative humidity of 55 % are maintained, unless stated otherwise. It is important to note that the adopted salt concentration is significantly higher than the current levels measured in Amsterdam canals. However, this elevated concentration is used to enhance the understanding of the potential degradation caused by salt crystallisation in the masonry of these historic structures and to accelerate the simulations. Additionally, it is plausible that these structures were exposed to such elevated salt concentrations during their centuries-old history, particularly prior to the construction of the seawater barriers around Amsterdam. It is also possible that they could experience similar elevated salt concentrations in the future due to potential impacts of climate change.

3.3. *Influence of boundary conditions*

Building on the numerical model of the case study described in Section 3.2, this section investigates four possible combinations of boundary conditions representing the surroundings of the masonry quay wall. These combinations are defined by two key factors: (1) the material of the capstone—either cementitious paste, which permits evaporation, or granite, which does not (modelled as a sealed surface); and (2) whether evaporation is allowed or not through the backfill. The resulting combinations are summarised in Table 2 and illustrated in Fig. 3.

The results of the simulations for these four models are presented in terms of c_s^s, the concentration of solid salt distribution within the wall section at steady state. Additionally, c_s^s is sampled at the specified points at the same depth but at different heights in the wall section illustrated in Fig. 4, to monitor its evolution throughout the simulation. These points are all positioned 3 cm deep within the wall and spaced vertically at intervals of 20 cm. Points A to D are positioned above the water level, point E is located precisely at the

Table 2
Summary of model variations investigated in terms of boundary conditions.

Model	Capstone Material	Capstone Evaporation	Backfill Evaporation
1	Cementitious	Yes	Yes
2	Cementitious	Yes	No
3	Granite	No	Yes
4	Granite	No	No

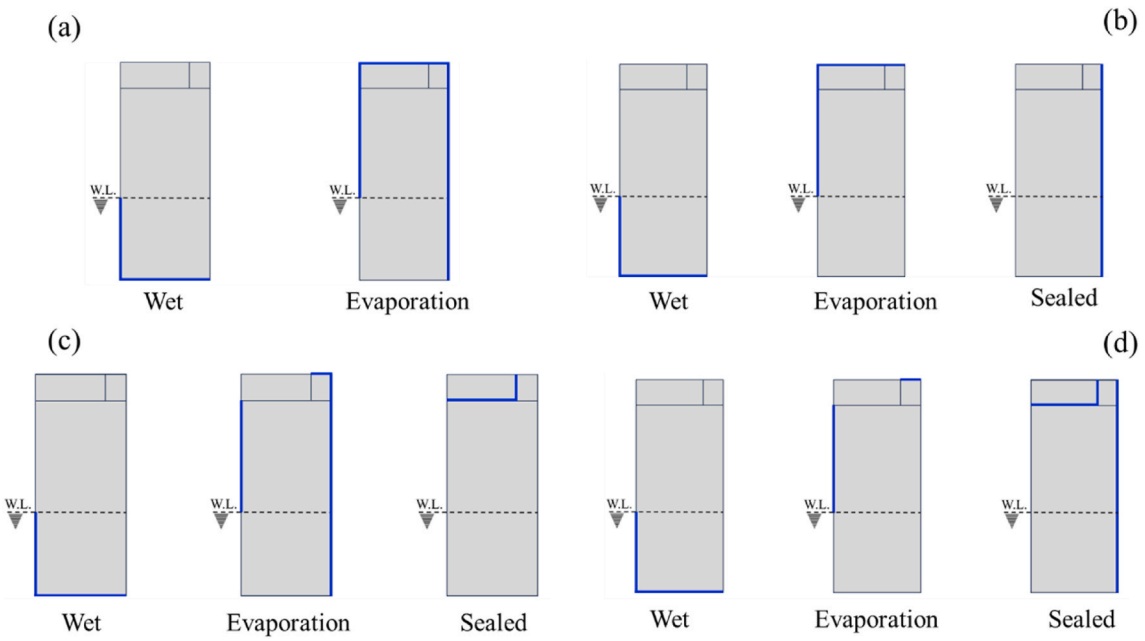

Fig. 3. Graphical depiction of boundary conditions in the investigated model variations: (a) Model 1; (b) Model 2; (c) Model 3 and (d) Model 4.

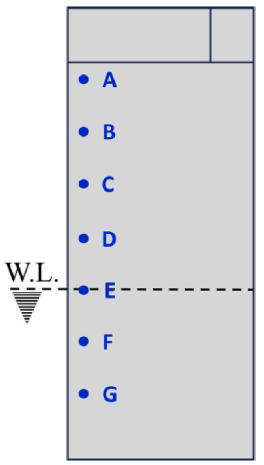

Fig. 4. Naming and location of the points in the wall section where the evolution of c_s^s i.e. the concentration of solid salt is monitored.

water level, and points F and G are situated below the water level. These results of all four models are provided in Figs. 5–8 respectively.

The responses of the four models reveal distinct trends in the distribution and progression of salt crystallisation under varying boundary conditions. Model 1 exhibits the broadest region affected by salt crystallisation, with significant accumulation near the surfaces where evaporation is facilitated (Fig. 5a). Its steady-state response is achieved after approximately 1200 h, following an activation phase of about 40 h and a prolonged variation phase (Fig. 5b). This highlights the influence of evaporation through both the wall-backfill interface and the capstone, which creates favourable conditions for widespread salt deposition.

Model 2, which restricts evaporation through the wall-backfill interface, demonstrates a thinner region of salt crystallisation

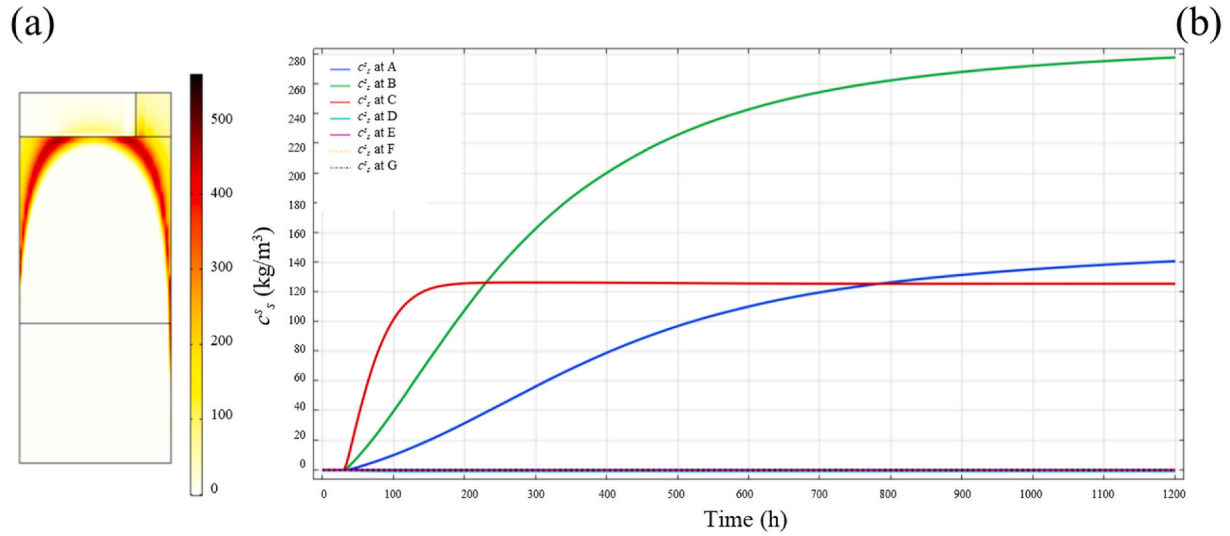

Fig. 5. Concentration of solid salt c_s^s in kg/m^3 for Model 1 with evaporation allowed thought the capstone and the backfill: (a) distribution across the wall section at steady state, and (b) evolution over time at different locations.

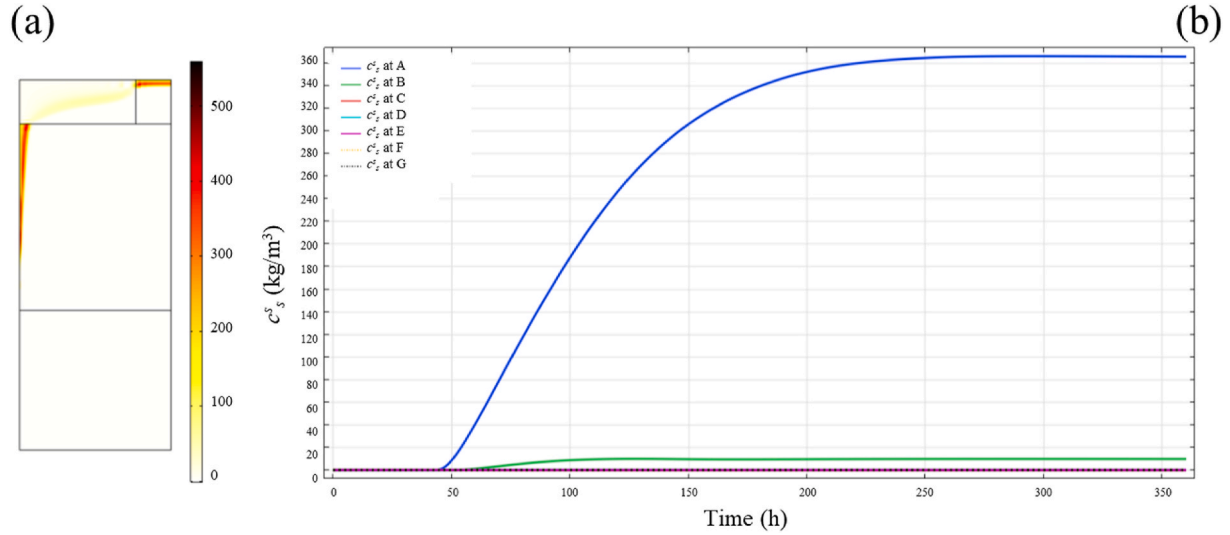

Fig. 6. Concentration of solid salt c_s^s in kg/m^3 for Model 2 with evaporation allowed thought the capstone and restricted thought the backfill: (a) distribution across the wall section at steady state, and (b) evolution over time at different locations.

compared to Model 1 (Fig. 5a). The steady-state response is achieved much faster, within approximately 250 h. The activation phase lasts around 45 h, slightly longer than Model 1, but the significantly shorter variation phase underscores the reduced impact of backfill evaporation on salt accumulation (Fig. 5b). The capstone, with its lower porosity as compared to the masonry, remains minimally affected in both models.

Model 3 shares similarities with Model 1, as it permits evaporation through the backfill. The CSS distribution map reveals a wide affected area, consistent with the influence of evaporation through multiple surfaces (Fig. 7a). However, the steady-state response is slightly delayed with respect to Model 1, requiring approximately 1400 h to stabilise. The activation phase is relatively short at around 35 h, but the prolonged variation phase indicates a more gradual accumulation of salt crystallisation ((Fig. 7b).

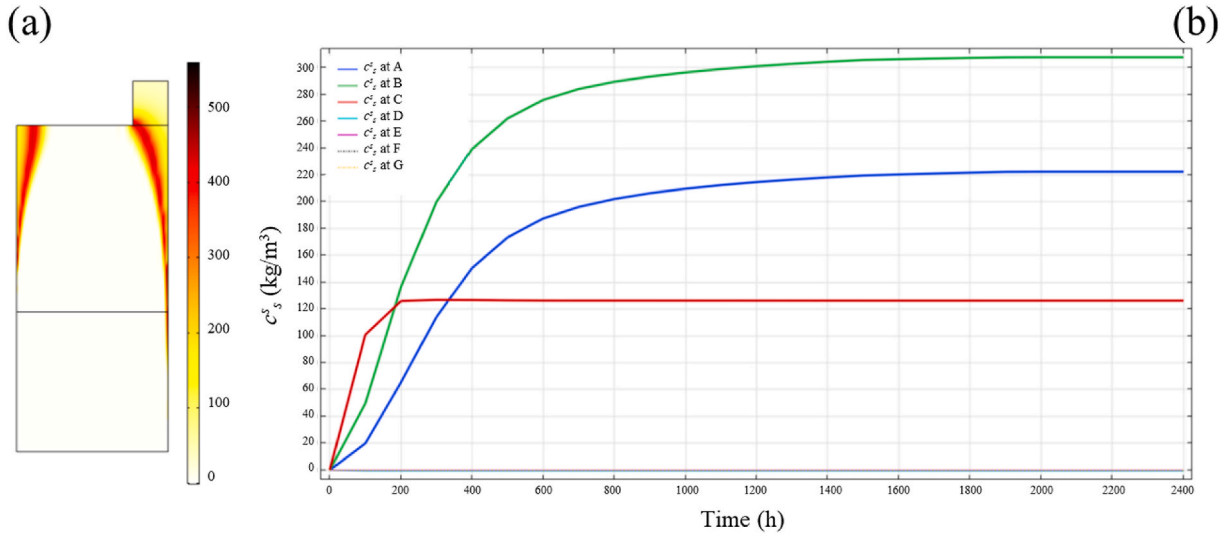

Fig. 7. Concentration of solid salt c_s^s in kg/m^3 for Model 3 with evaporation restricted thought the capstone and allowed thought the backfill: (a) distribution across the wall section at steady state, and (b) evolution over time at different locations.

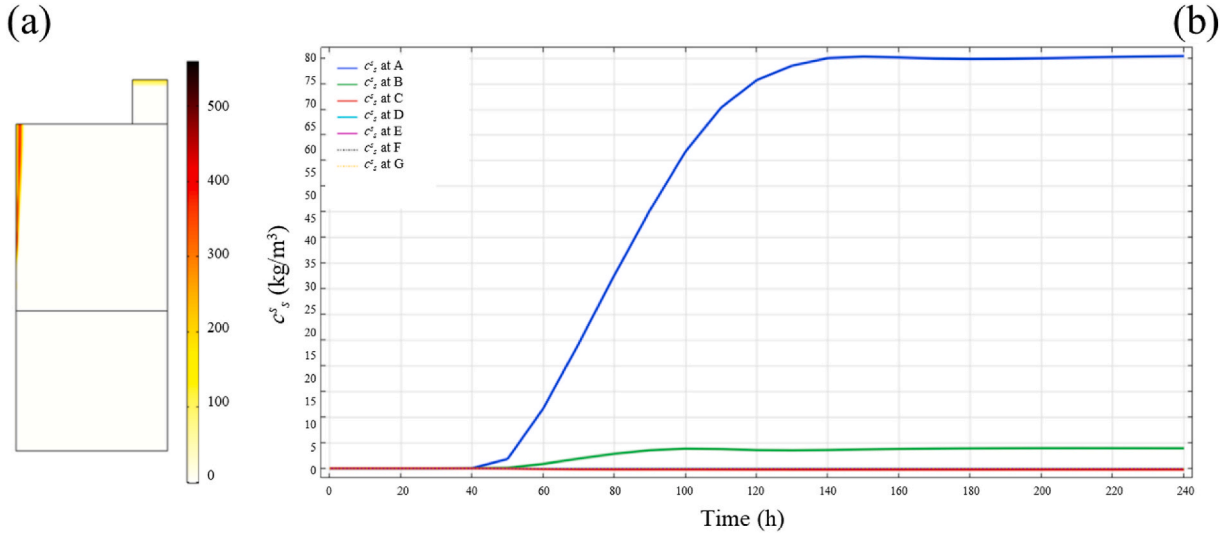

Fig. 8. Concentration of solid salt c_s^s in kg/m^3 for Model 4 with evaporation restricted thought both the capstone and the backfill: (a) distribution across the wall section at steady state, and (b) evolution over time at different locations.

In contrast, Model 4, which restricts evaporation through both the capstone and the backfill, presents the thinnest crystallisation region among all models (Fig. 8a). The steady-state response is achieved rapidly, within approximately 140 h. The activation phase lasts around 40 h, while the brief variation phase reflects the limited pathways for evaporation (Fig. 8b). This highlights the effectiveness of sealed surfaces in minimising salt crystallisation and accelerating the attainment of steady-state conditions.

Overall, the models illustrate the significant influence of boundary conditions on the extent and dynamics of salt crystallisation. Allowing evaporation through the backfill and capstone results in broader affected areas and longer times to reach steady state, while restricting evaporation through these surfaces significantly reduces salt accumulation and accelerates stabilisation. Despite exhibiting the lowest accumulation of salt among all four models, the boundary conditions of Model 4 were selected for all future simulations reported in this paper. This decision was based on personal communications with *Ingenieursbureau Amsterdam* [61], which revealed that these conditions are prevalent in the most vulnerable historical quays of Amsterdam.

3.4. Assessing model sensitivity

To assess the sensitivity of Model 4, two additional simulations were performed with salt concentrations in the canal water assumed to be 0.035 and 0.045 kg/l, as opposed to 0.04 kg/l in the results reported in Section 3.3. Similarly, two further simulations were carried out, assuming total masonry open porosity values of 24 % and 28 %, compared to the baseline value of 26 % used in Section 3.3. Figs. 9 and 10 report the c_s^s values for these simulations at various locations along the thickness of the wall at the same height as point A, where the highest c_s^s values in the wall section were observed in the simulations for all models, including Model 4.

While the overall distribution of c_s^s on the wall section remained approximately the same across all four simulations, these sensitivity analyses revealed distinct trends in the time required to reach steady-state solutions and the maximum evaluated c_s^s values. Increasing the salt concentration to 0.045 kg/l reduced the time to reach the steady-state solution to approximately 180 h and resulted in a slight increase in the maximum c_s^s value, which reached 440 kg/m^3. Conversely, reducing the salt concentration to 0.035 kg/l significantly increased the time to steady state to approximately 1200 h and lowered the maximum c_s^s value to 290 kg/m^3. In the simulations varying masonry open porosity, increasing the porosity to 28 % extended the time required to reach the steady-state solution significantly, to approximately 2000 h. This increase in porosity also reduced the maximum c_s^s value to 250 kg/m^3. Conversely, reducing the porosity to 24 % resulted in a steady-state solution being reached in approximately 180 h, similar to the baseline. This reduction in porosity was accompanied by a slight increase in the maximum c_s^s value, which reached 390 kg/m^3 (Fig. 10). For reference, the results previously reported for Model 4 showed a maximum CSS value of 420 kg/m^3, with the steady-state solution reached after approximately 240 h (Fig. 8).

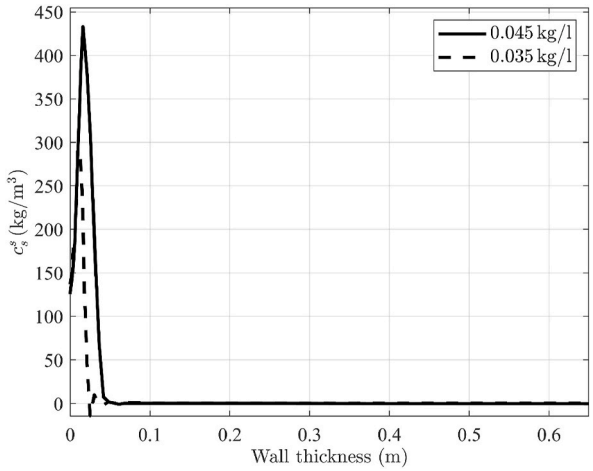

Fig. 9. Value of c_s^s along the wall thickness (at the height of location A in the wall section, see Fig. 4) for canal water salt concentrations of 0.045 and 0.035 kg/l.

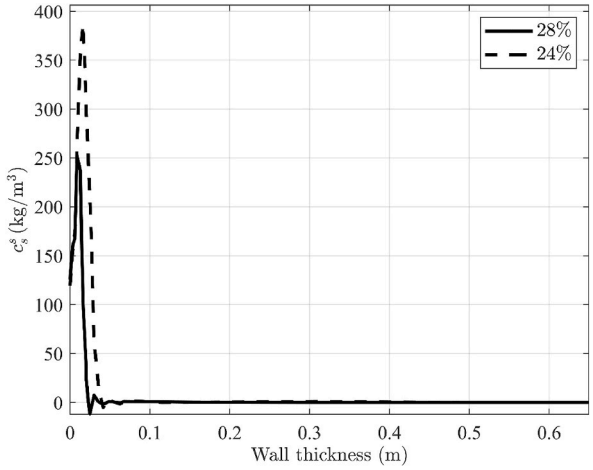

Fig. 10. Value of c_s^s along the wall thickness (at the height of location A in the wall section, see Fig. 4) for total masonry open porosity values of 28 % and 24 %.

3.5. Modelling masonry texture

Until now, the masonry wall of the quay has been modelled as a homogeneous continuum. In this section, the potential impact of explicitly modelling masonry texture, i.e. accounting for individual bricks and mortar, is investigated. The first step in this process is defining the bond pattern that can be represented in a 2D sectional model, such as the one used in this study. This task is non-trivial, given that quay walls are multi-wythe structures that typically extend hundreds of metres in length. Based on personal communication with an expert mason [62], a possible arrangement of bricks along the thickness and height of the wall was obtained [48,52].

Fig. 11 presents the front view of the brickwork pattern, while Fig. 12 shows the top view of the four distinct repeating brick layers identified in the pattern (designated as 1, 2, 1*, and 3). From this information, three 2D cross-sectional brickwork patterns were identified and among these the most recurring sectional masonry texture along the length of the quay wall was therefore selected for further cross-sectional analysis, as illustrated in Fig. 13a. Dimensions of bricks and mortar joints were considered based on the observations from the case study analysed in Ref. [57]. Brick dimensions were 210 x 100 × 50 mm. A uniform joint thickness of 10 mm was considered, although large variations were observed within the mortar joints thickness. Fig. 13b depicts the mesh adopted for the numerical model incorporating masonry texture. This mesh uses triangular elements, in contrast to the quadrilateral elements used in the homogeneous model. In this preliminary attempt to explore the potential of modelling masonry texture, the bricks and mortar are assigned the properties previously used for masonry and cementitious materials, respectively (Table 1). The Model 4 variation (Fig. 3) is adopted once again for the boundary conditions.

The steady-state results of the homogeneous and textured models, as compared in Fig. 14, reveal distinct differences in the extent of salt crystallisation within the wall. In the homogeneous model, the crystallised salt penetrates to a maximum depth of approximately 4 cm whereas in the textured model, it reaches a depth of about 13 cm (Fig. 14a). A wider portion of the wall is observed to be affected by

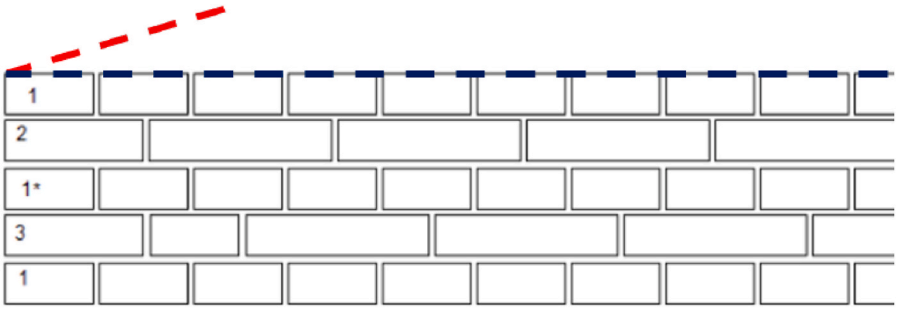

Fig. 11. Front view of a commonly used brickwork bond pattern in Dutch quay walls. The bond pattern consists of a repetition of four layers. The red and blue lines indicate the top view orientations of the layers depicted in Fig. 11 [62].

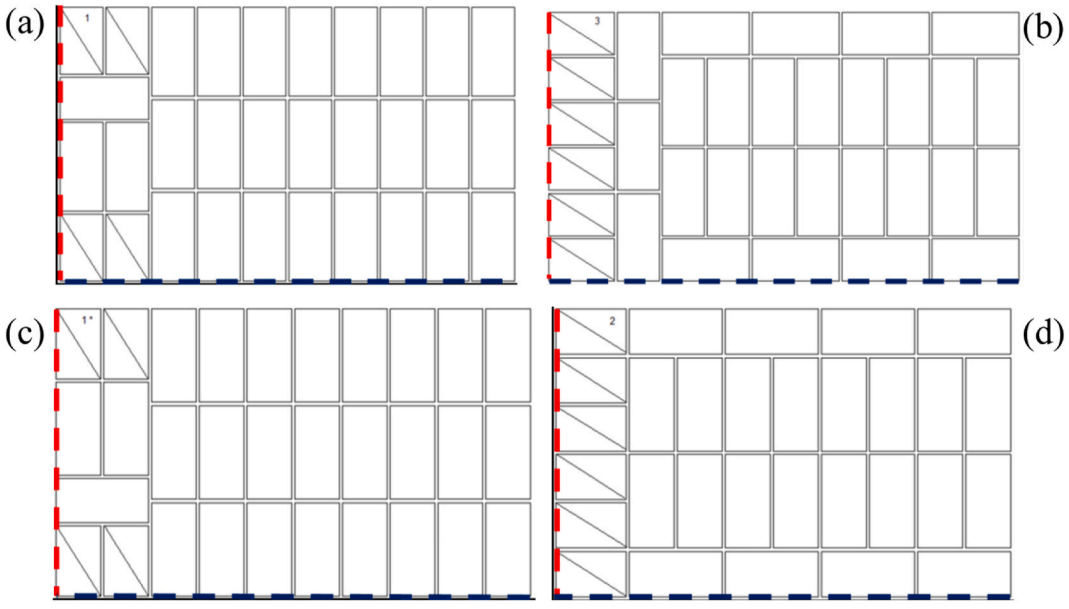

Fig. 12. Top view of the four distinct repeating brick layers identified in the bond pattern illustrated in Fig. 11: (a) Layer 1: (b) Layer 3; (c) Layer 1*, and (d) Layer 3 [62].

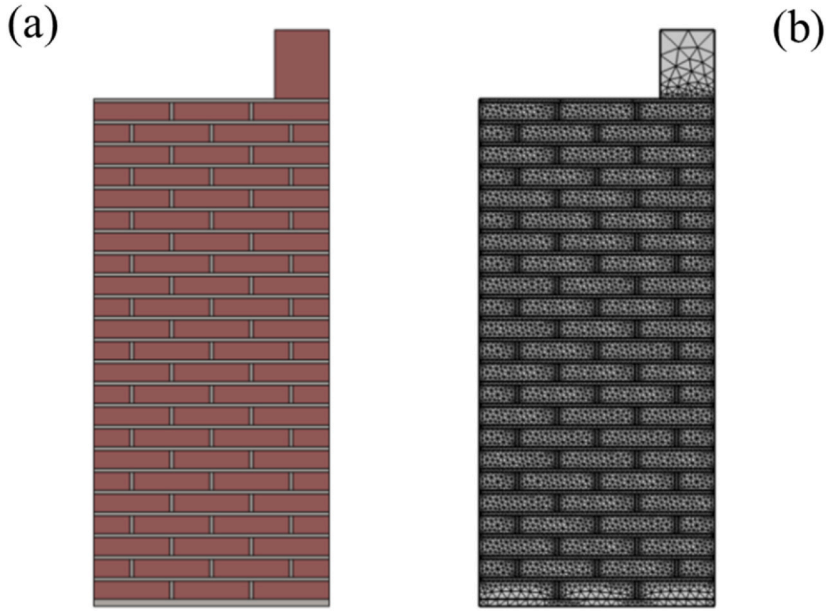

Fig. 13. (a) Most recurring sectional masonry texture configuration along the length of the quay wall and (b) mesh adopted for the numerical model accounting for masonry texture.

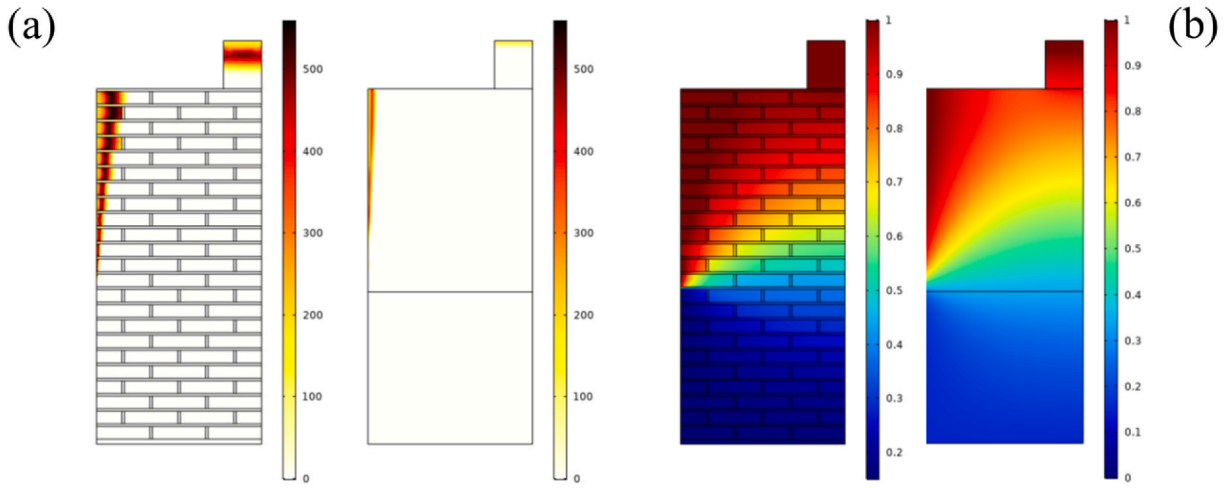

Fig. 14. Comparison of the response between models considering masonry as a homogeneous continuum and those incorporating masonry texture, in terms of: (a) c_s^s and (b) ω/ω_{sat}.

crystallisation in the textured model overall. Furthermore, the ω/ω_{sat} contour plots demonstrate that the wall portion near the crystallisation threshold is significantly larger in the textured model (Fig. 14b). The maximum c_s^s in the textured model also reaches 540 kg/m^3, a value approaching the saturation limit of 560 kg/m^3 and substantially higher than the maximum c_s^s of 420 kg/m^3 observed in the homogeneous model (Fig. 14a).

The temporal evolution of c_s^s (plotted in Fig. 15 at the location of point A in the wall section) further highlights differences between the two models. The homogeneous model exhibits an activation phase lasting approximately 40 h, followed by a variation phase that reaches steady-state conditions after 140 h. During this time, the maximum registered c_s^s value is approximately 80 kg/m^3. In contrast, the textured model shows a significantly delayed response, with an activation phase of approximately 160 h, followed by a variation phase that stabilises at steady state after about 600 h. The maximum registered c_s^s value in the textured model reaches 350 kg/m^3, reflecting a much greater accumulation of salt close to the full saturation of the masonry pores, as dictated by the adopted porosity. This behaviour is to be expected, as the textured model introduces a porosity gradient between the brick and mortar phases.

The textured model demonstrates a better ability to capture the nuanced behaviour of masonry under salt crystallisation. Despite its significantly higher computational cost, requiring approximately 600 h to reach steady-state compared to just 160 h for the

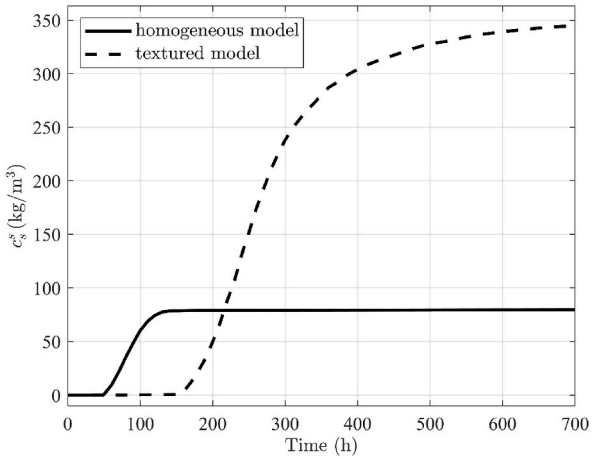

Fig. 15. Comparison of the temporal evolution of c_s^s between the models considering masonry as a homogeneous continuum and incorporating masonry texture (c_s^s is plotted at location A in the wall section, see Fig. 4).

homogeneous model, its exhibits potentially more degrading effects of salt crystallisation on masonry of the quay. Consequently, this model is carried forward for preliminary simulations of multiple weathering cycles in section 3.6.

3.6. Long-term effects of weathering

A preliminary attempt is made at simulating the long terms of weathering in this section. The long-term effects of weathering can be simulated by varying environmental conditions, such as seasonal cycles or daily fluctuations in temperature and humidity. In this study, since NaCl salt is not significantly influenced by temperature variations, the level of ambient relative humidity (RH) was varied to examine its impact. This preliminary work investigates the effects of sequentially applying three idealised ambient humidity conditions, capturing the accumulation of salt during phases of crystallisation, dissolution, and subsequent recrystallisation. Three time intervals were considered: the first with RH = 55 % maintained for 300 h; the second with RH = 85 % for 20 h; and the third returning to RH = 55 % for another 300 h. Fig. 16 illustrates the variation of c_s^s during these intervals, revealing that the distribution of c_s^s is influenced not only by the time required to reach steady-state conditions but also by the sequence of humidity events: the accumulation of salt is narrowing around the peak value after the dissolution phase. It is important to note that this analysis is preliminary, and potential variations in porosity, tortuosity, and the degree of pore filling due to mechanical damage must be taken into account when interpreting these results [36].

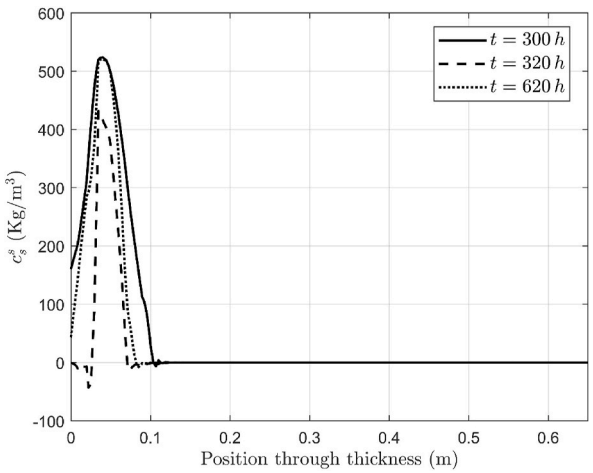

Fig. 16. Value of c_s^s along the wall thickness (at the height of location A in the wall section, see Fig. 4) for the steady state and second weathering cycle.

4. Estimation of the effective Young's modulus

The results from the numerical models presented in the previous sections demonstrate that salt crystallisation can occur in the case study under investigation, with a penetration depth of approximately 13 cm when considering masonry texture (Fig. 14a). This depth could increase further under varying boundary conditions, although such scenarios are less common in practice (Section 3.3). Given that salt (NaCl) has a significantly higher Young's modulus than masonry, its potential impact on the experimental evaluation of masonry's Young's modulus is examined in this section. Specifically, considering a representative elementary volume (REV) located around a point within a brick subjected to the abovementioned salt crystallisation accumulation, this analysis investigates whether this phenomenon could contribute to the through-thickness effects observed in Ref. [57] and summarised in Section 1.

To estimate the effective Young's modulus of a composite material, the Rule of Mixtures is commonly used as an initial approach, providing both an upper and a lower bound. These bounds account for the contributions of individual constituent phases based on their respective volume fractions. Assuming a uniform strain distribution (Voigt model [63]) yields the upper bound $E_{eff,\ upper}$, while assuming a uniform stress distribution (Reuss model [64]) yields the lower bound $E_{eff,\ lower}$, thereby offering initial estimates of the composite modulus.

$$E_{eff.upper} = V_f \cdot E_{mas} + \left(1 - V_f\right) \cdot E_{salt} \tag{7}$$

$$E_{eff.lower} = \left(\frac{V_f}{E_{mas}} + \frac{1 - V_f}{E_{salt}}\right)^{-1} \tag{8}$$

being E_{brick} the Young's modulus of the brick, E_{salt} the Young's modulus of NaCl salt. V_f is the volume fraction of the brick matrix, defined as:

$$V_f = \frac{V_{br}}{V_{br} + V_{salt}} \tag{9}$$

where $V_{br} = 1 - \phi_{0,br}$ and $V_{salt} = \phi_{0,br} - \phi_{eff,br}$ with $\phi_{0,br}$ representing the initial porosity and $\phi_{eff,br}$ the final (unfilled) porosity of bricks. While this definition can certainly be refined using formulations in Refs. [65,66], a straightforward improvement can be achieved by applying the model proposed by Boccaccini and Fan [67]. This model predicts the effective Young's modulus of porous materials by incorporating topological parameters, providing an intermediate estimate between the estimates of equations (7) and (8). The rule is expressed as:

$$E_{eff,Boccaccini\ \&\ Fan} = E_{Matrix} \cdot f_c \tag{10}$$

where E_{brick} represents the Young's modulus of the pore-free brick material, and f_c is the volume fraction of the brick phase. This volume fraction accounts for porosity and phase distribution, enabling a more refined estimation and it is defined as:

$$f_c = \frac{\left(1 - \phi_{0,br}\right)^2 \cdot R_{mp}}{\phi_{0,br} + \left(1 - \phi_{0,br}\right) \cdot R_{mp}} \tag{11}$$

where R_{mp} represents the particle size ratio between the matrix and pore phases. This model can be adapted to predict the effective Young's modulus of porous materials where the pores are partially or fully filled with a secondary material, such as salt. The modified rule is expressed as:

$$E_{eff} = E_{\text{matrix}} \cdot f_c^{brick} + E_{\text{salt}} \cdot f_c^{\text{salt}} \tag{12}$$

where f_c^{brick} and f_c^{salt} are the continuous volume fraction of the brick matrix and salt phase respectively computed as:

$$f_c^{\text{brick}} = \frac{V_{\text{brick}}^2 \cdot R_{bs}}{V_{\text{brick}} + V_{\text{salt}} \cdot R_{bs}} \tag{13}$$

$$f_c^{\text{salt}} = \frac{V_{\text{salt}}^2 \cdot R_{bs}}{V_{\text{salt}} + V_{\text{brick}} \cdot R_{bs}} \tag{14}$$

where the particle size ratio R_{bs} is a geometric parameter that reflects the relative sizes of the brick and salt phases. In the absence of experimental evidence, an initial guess for R_{bs} could be set at 1.5.

Fig. 17 presents the distribution of normalised Young's modulus of bricks across the walls section, calculated using the three aforementioned estimates. The normalised value is obtained as the ratio between the effective Young's modulus and the initial Young's modulus of the bricks prior to simulating any weathering effects. Due to the presence of salt, bricks exposed to the canal face (external side) may exhibit an increase in Young's modulus. According to the lower-bound estimate $E_{eff,\ lower}$, a minimum increase of approximately 40 % is expected (Fig. 17a), while the upper-bound estimate $E_{eff,\ upper}$ predicts a maximum increase of around 600 % (Fig. 17b). The model by Boccaccini and Fan i.e. $E_{eff,\ Boccaccini\ and\ Fan}$ suggests an intermediate increase of approximately 200 % ((Fig. 17c).

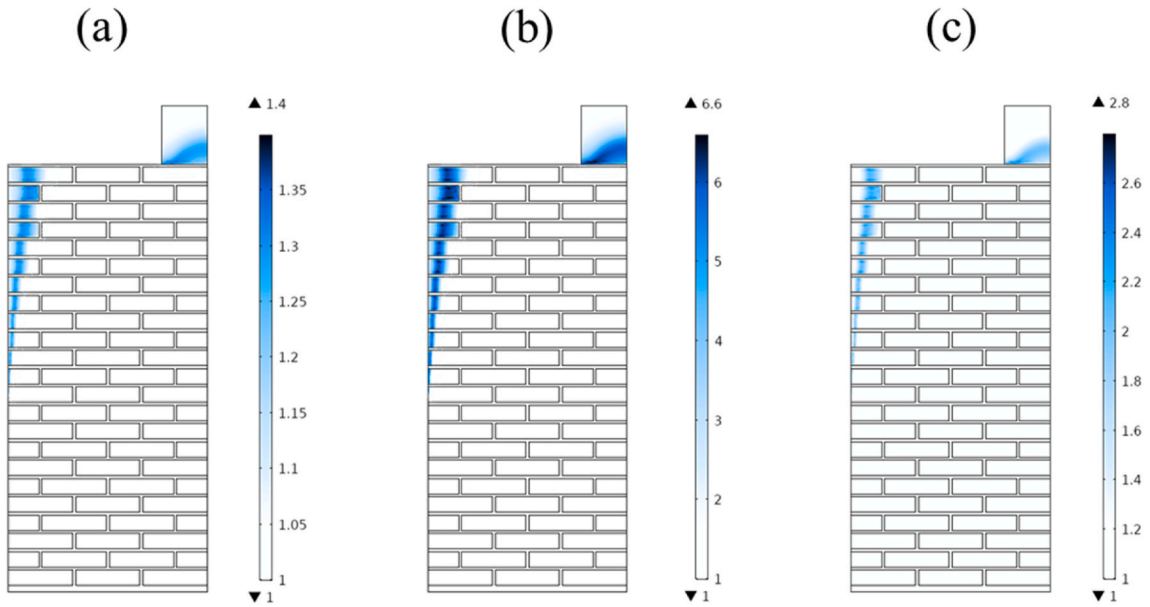

Fig. 17. Normalised Young's modulus of bricks using (a) Voigt, (b) Reuss, and (c) Boccaccini and Fan models. (The plot refers exclusively to the brick geometrical domain)

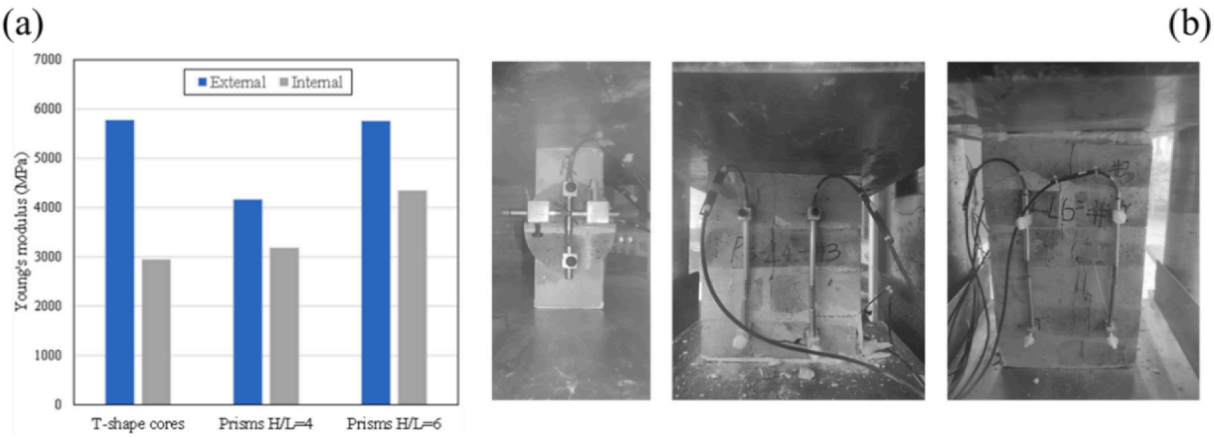

Fig. 18. (a) Young's modulus of masonry for the external and internal portions of a masonry bridge pillar in Amsterdam estimated from compression tests were performed on various specimens, including T-shaped cores and prisms with height-to-length ratios of 4 and 6 (b) (Figure adapted from Ref. [57]).

In a qualitative sense, these findings align with the experimental observations of the "through thickness effect" in Ref. [57] which partly motivated this study, as shown in Fig. 18. Despite differences in structural typology (quay wall and pillar of an arch bridge), it can be assumed that the exposure conditions and masonry type are comparable, given their similar locations and the likelihood of being constructed around the same period. The extensive experimental campaign included the estimation of the Young's modulus through uniaxial compression tests on T-shaped cores and masonry prisms with varying height-to-length ratios. In all cases, specimens extracted from the external side of the pillar, exposed to canal water, exhibited a higher Young's modulus compared to those from the internal side, with an increase ranging from 30 % to 100 %.

5. Concluding remarks

This study presents a numerical investigation of salt crystallisation-induced weathering in masonry earth-retaining walls, with a specific focus on historic quay walls in the city centre of Amsterdam, a UNESCO Heritage site. The modelling results demonstrate that.

- Boundary conditions significantly influence both the rate and extent of salt crystallisation. The presence of evaporation pathways through the backfill and capstone extend the affected region and delay steady-state conditions. Sealed surfaces restrict, but do not fully prevent, salt crystallisation.
- Explicitly accounting for masonry texture in the numerical model yields a deeper and more extensive build-up of crystallised salt, underscoring its importance in evaluating long-term deterioration
- Preliminary exploration of long-term weathering effects, achieved by incorporating variations in relative humidity, indicates that salt accumulation can progressively increase over multiple cycles. This highlights the need for continuous, rather than piecewise, modelling of such variations as done in this paper to capture the cumulative impact of environmental exposure, particularly as environmental variations become increasingly exacerbated by climate change.
- An initial assessment of how salt crystallisation could affect the effective Young's modulus of the masonry of the quay suggests that salt deposition within pores can significantly increase Young's modulus, especially in regions exposed to canal water. These findings align qualitatively with experimental observations of through-thickness variations in Young's modulus experimentally recorded on samples extracted from a historical masonry bridge pillar of the same masonry type, under similar environmental conditions to Amsterdam's historic quays.

To build on these findings and address the current limitations of the study, future research should focus on.

- Refining the simulations by carrying out thermo-hygro-mechanical characterisation to assess the input parameters required for the modelling approach; integrating measured variations in relative humidity, and exploring a broader range of masonry textures.
- Improving the stability and quality of the analysis by employing the staggered approach proposed in Ref. [38]: given the relatively slow timescales of these phenomena, this methodology provides a robust means of evaluating the cumulative effects of crystallised salt over time, offering a more accurate representation of long-term material degradation and mechanical evolution.

Based on the outcomes of these investigations, the structural implications of salt crystallisation should be incorporated into assessment frameworks, moving beyond idealised environmental conditions to ensure a more realistic evaluation of long-term performance. In conclusion, this study serves as a preliminary effort to identify the parameters influencing salt-induced degradation in masonry quay walls, laying the groundwork for more comprehensive investigations in the future.

CRediT authorship contribution statement

Satyadhrik Sharma: Writing – review & editing, Writing – original draft, Visualization, Formal analysis, Conceptualization. **Rita Esposito:** Writing – review & editing, Project administration, Funding acquisition, Conceptualization. **Antonio Maria D'Altri:** Writing – review & editing, Software, Methodology. **Giovanni Castellazzi:** Writing – review & editing, Visualization, Software, Methodology, Conceptualization.

Declaration of competing interest

The authors declare that they have no known competing financial interests or personal relationships that could have appeared to influence the work reported in this paper.

Acknowledgements

The first two authors developed this work in the context of the project "Structural analyses and material characterisation for the assessment of masonry urban infrastructure" financially supported by the municipality of Amsterdam via the Amsterdam Institute for Advanced Metropolitan Solutions (AMS). Mr Alberto Gagliardi is also acknowledged for his support.

Data availability

Data will be made available on request.

References

[1] Gemeente Amsterdam, Actieplan Bruggen en Kademuren 2023-2026, 2022. Amsterdam, the Netherlands.
[2] M.P. O Reilly, D.I. Bush, K.C. Brady, W. Powrie, The stability of drystone retaining walls on highways, Proceedings of the Institution of Civil Engineers - Municipal Engineer 133 (1999) 101–107, https://doi.org/10.1680/imuen.1999.31763.
[3] P.F. McCombie, C. Mundell, A. Heath, P. Walker, Drystone retaining walls: ductile engineering structures with tensile strength, Eng. Struct. 45 (2012) 238–243, https://doi.org/10.1016/j.engstruct.2012.06.046.
[4] A. Hough, Assessment of historical railway retaining walls, Proceedings of the Institution of Civil Engineers - Transport 147 (2001) 217–221, https://doi.org/10.1680/tran.2001.147.4.217.
[5] N. Odent, Recensement des ouvrages de soutènement en bordure du réseau routier national, 34, Ouvrage d'Art, 2000, pp. 15–18.
[6] M.J. DeMarco, R.J. Barrows, S. Lewis, NPS retaining wall inventory and assessment program (WIP): 3,500 walls later, in: Earth Retention Conference 3, American Society of Civil Engineers, 2010, pp. 870–877, https://doi.org/10.1061/41128(384)87. Reston, VA.
[7] V.P. Gupta, N.K. Lohani, Treatment and repair of partially damaged retaining walls in hills, Indian Highways 10 (1982) 20–28.

[8] A.S. Arya, V.P. Gupta, Retaining wall for hill roads, Indian Road Congress Journal 44 (1983) 291–326.
[9] D.R. Easterling, G.A. Meehl, C. Parmesan, S.A. Changnon, T.R. Karl, L.O. Mearns, Climate extremes: observations, modeling, and impacts, Science 289 (1979) 2068–2074, https://doi.org/10.1126/science.289.5487.2068, 2000.
[10] K. Trenberth, Changes in precipitation with climate change, Clim. Res. 47 (2011) 123–138, https://doi.org/10.3354/cr00953.
[11] M.G. Donat, A.L. Lowry, L.V. Alexander, P.A. O'Gorman, N. Maher, More extreme precipitation in the world's dry and wet regions, Nat. Clim. Change 6 (2016) 508–513, https://doi.org/10.1038/nclimate2941.
[12] E.M. Fischer, R. Knutti, Anthropogenic contribution to global occurrence of heavy-precipitation and high-temperature extremes, Nat. Clim. Change 5 (2015) 560–564, https://doi.org/10.1038/nclimate2617.
[13] F. Homaei, M. Yazdani, Seismic fragility, loss, and resiliency of old railway masonry arch bridges under near-field ground motion, Sustain Resilient Infrastruct (2025) 1–28, https://doi.org/10.1080/23789689.2025.2456362.
[14] V. Sarhosis, S. De Santis, G. de Felice, A review of experimental investigations and assessment methods for masonry arch bridges, Structure and Infrastructure Engineering 12 (2016) 1439–1464, https://doi.org/10.1080/15732479.2015.1136655.
[15] Y. Zhang, L. Macorini, B.A. Izzuddin, Numerical investigation of arches in brick-masonry bridges, Structure and Infrastructure Engineering 14 (2018) 14–32, https://doi.org/10.1080/15732479.2017.1324883.
[16] L. Pelà, A. Aprile, A. Benedetti, Seismic assessment of masonry arch bridges, Eng. Struct. 31 (2009) 1777–1788, https://doi.org/10.1016/j.engstruct.2009.02.012.
[17] L. Pelà, A. Aprile, A. Benedetti, Comparison of seismic assessment procedures for masonry arch bridges, Constr. Build. Mater. 38 (2013) 381–394, https://doi.org/10.1016/j.conbuildmat.2012.08.046.
[18] D. Addessi, C. Gatta, M. Nocera, D. Liberatore, Nonlinear dynamic analysis of a masonry arch bridge accounting for damage evolution, Geosciences 11 (2021) 343, https://doi.org/10.3390/geosciences11080343.
[19] M. Rota, A. Pecker, D. Bolognini, R. Pinho, A methodology for seismic vulnerability of masonry arch bridge walls, J. Earthq. Eng. 9 (2005) 331–353, https://doi.org/10.1142/S1363246905002432.
[20] T. Forgács, V. Sarhosis, S. Ádány, Shakedown and dynamic behaviour of masonry arch railway bridges, Eng. Struct. 228 (2021) 111474, https://doi.org/10.1016/j.engstruct.2020.111474.
[21] B. Sobczyk, Ł. Pyrzowski, M. Miśkiewicz, Computational modelling of historic masonry railroad arch bridges, Comput. Struct. 291 (2024) 107214, https://doi.org/10.1016/j.compstruc.2023.107214.
[22] R.J. Flatt, F. Caruso, A.M.A. Sanchez, G.W. Scherer, Chemo-mechanics of salt damage in stone, Nat. Commun. 5 (2014) 4823, https://doi.org/10.1038/ncomms5823.
[23] B. Lubelli, I. Rörig-Daalgard, A.M. Aguilar, M. Aškrabić, K. Beck, C. Bläuer, V. Cnudde, A.M. D'Altri, H. Derluyn, J. Desarnaud, T. Diaz Gonçalves, R. Flatt, E. Franzoni, S. Godts, D. Gulotta, R. van Hees, I. Ioannou, A. Kamat, T. De Kock, B. Menendez, S. de Miranda, C. Nunes, E. Sassoni, N. Shahidzadeh, H. Siedel, Z. Slížková, M. Stefanidou, M. Theodoridou, R. Veiga, V. Vergès-Belmin, Recommendation of RILEM TC 271-ASC: new accelerated test procedure for the assessment of resistance of natural stone and fired-clay brick units against salt crystallization, Mater. Struct. 56 (2023) 101, https://doi.org/10.1617/s11527-023-02158-0.
[24] C. Gentilini, E. Franzoni, S. Bandini, L. Nobile, Effect of salt crystallisation on the shear behaviour of masonry walls: an experimental study, Constr. Build. Mater. 37 (2012) 181–189, https://doi.org/10.1016/j.conbuildmat.2012.07.086.
[25] A. Gabrielli, G. Ugolotti, G. Masi, E. Sassoni, Resistance of consolidated lime mortars to freeze–thaw and salt crystallization cycles by different accelerated durability tests, Mater. Struct. 57 (2024) 70, https://doi.org/10.1617/s11527-024-02361-7.
[26] E. Franzoni, C. Gentilini, G. Graziani, S. Bandini, Towards the assessment of the shear behaviour of masonry in on-site conditions: a study on dry and salt/water conditioned brick masonry triplets, Constr. Build. Mater. 65 (2014) 405–416, https://doi.org/10.1016/j.conbuildmat.2014.05.002.
[27] B. Lubelli, A.M. Aguilar, K. Beck, T. De Kock, J. Desarnaud, E. Franzoni, D. Gulotta, I. Ioannou, A. Kamat, B. Menendez, I. Rörig-Dalgaard, E. Sassoni, A new accelerated salt weathering test by RILEM TC 271-ASC: preliminary round robin validation, Mater. Struct. 55 (2022) 238, https://doi.org/10.1617/s11527-022-02067-8.
[28] A. Nazerigivi, B. Ghiassi, G. Vasconcelos, A. Dionísio, Numerical modeling of salt crystallization in masonry: a critical review of developed numerical models, J. Cult. Herit. 70 (2024) 143–156, https://doi.org/10.1016/j.culher.2024.08.018.
[29] R. Ramirez, B. Ghiassi, P. Pineda, P.B. Lourenço, Simulation of moisture transport in fired-clay brick masonry structures accounting for interfacial phenomena, Build. Environ. 228 (2023) 109838, https://doi.org/10.1016/j.buildenv.2022.109838.
[30] R. Ramirez, B. Ghiassi, P. Pineda, P.B. Lourenço, Hygro-thermo-mechanical analysis of brick masonry walls subjected to environmental actions, Appl. Sci. 13 (2023) 4514, https://doi.org/10.3390/app13074514.
[31] M. Koniorczyk, D. Gawin, Heat and moisture transport in porous building materials containing salt, J. Build. Phys. 31 (2008) 279–300, https://doi.org/10.1177/1744259107088003.
[32] M. Koniorczyk, D. Gawin, Numerical modeling of salt transport and precipitation in non-isothermal partially saturated porous media considering kinetics of salt phase changes, Transport Porous Media 87 (2011) 57–76, https://doi.org/10.1007/s11242-010-9668-7.
[33] M. Koniorczyk, D. Gawin, Modelling of salt crystallization in building materials with microstructure – poromechanical approach, Constr. Build. Mater. 36 (2012) 860–873, https://doi.org/10.1016/j.conbuildmat.2012.06.035.
[34] M. Koniorczyk, D. Gawin, B.A. Schrefler, Multiphysics model for spalling prediction of brick due to in-pore salt crystallization, Comput. Struct. 196 (2018) 233–245, https://doi.org/10.1016/j.compstruc.2017.10.013.
[35] H. Derluyn, P. Moonen, J. Carmeliet, Deformation and damage due to drying-induced salt crystallization in porous limestone, J. Mech. Phys. Solid. 63 (2014) 242–255, https://doi.org/10.1016/j.jmps.2013.09.005.
[36] G. Castellazzi, C. Colla, S. de Miranda, G. Formica, E. Gabrielli, L. Molari, F. Ubertini, A coupled multiphase model for hygrothermal analysis of masonry structures and prediction of stress induced by salt crystallization, Constr. Build. Mater. 41 (2013) 717–731, https://doi.org/10.1016/j.conbuildmat.2012.12.045.
[37] S. de Miranda, A.M. D'Altri, G. Castellazzi, Modeling environmental ageing in masonry strengthened with composites, Eng. Struct. 201 (2019) 109773, https://doi.org/10.1016/j.engstruct.2019.109773.
[38] G. Castellazzi, A.M. D'Altri, S. de Miranda, H. Emami, L. Molari, F. Ubertini, A staggered multiphysics framework for salt crystallization-induced damage in porous building materials, Constr. Build. Mater. 304 (2021) 124486, https://doi.org/10.1016/j.conbuildmat.2021.124486.
[39] A.M. D'Altri, S. de Miranda, K. Beck, T. De Kock, H. Derluyn, Towards a more effective and reliable salt crystallisation test for porous building materials: predictive modelling of sodium chloride salt distribution, Constr. Build. Mater. 304 (2021) 124436, https://doi.org/10.1016/j.conbuildmat.2021.124436.
[40] G. Castellazzi, S. de Miranda, L. Grementieri, L. Molari, F. Ubertini, Multiphase model for hygrothermal analysis of porous media with salt crystallization and hydration, Mater. Struct. 49 (2016) 1039–1063, https://doi.org/10.1617/s11527-015-0557-y.
[41] J. Choo, W. Sun, Cracking and damage from crystallization in pores: coupled chemo-hydro-mechanics and phase-field modeling, Comput. Methods Appl. Mech. Eng. 335 (2018) 347–379, https://doi.org/10.1016/j.cma.2018.01.044.
[42] M. Korff, M.-J. Hemel, D.J. Peters, Collapse of the Grimburgwal, a historic quay in Amsterdam, The Netherlands, Proceedings of the Institution of Civil Engineers - Forensic Engineering 175 (2022) 96–105, https://doi.org/10.1680/jfoen.21.00018.
[43] M.-J. Hemel, D.J. Peters, T. Schweckendiek, S.N. Jonkman, Reliability updating for lateral failure of historic quay walls, Georisk 18 (2024) 882–903, https://doi.org/10.1080/17499518.2024.2302141.
[44] M. Mirra, G. Pagella, M. Lee, W. Gard, G. Ravenshorst, J.-W. van de Kuilen, Characterisation of bacterial decay effects on wooden foundation piles across various historical periods, Constr. Build. Mater. 421 (2024) 135670, https://doi.org/10.1016/j.conbuildmat.2024.135670.
[45] M. Felicita, G. Pagella, G. Ravenshorst, M. Mirra, J.-W. van de Kuilen, Assessment of in-situ stress distribution and mechanical properties of wooden foundation piles instrumented with distributed fiber optic sensors (DFOS), Case Stud. Constr. Mater. 20 (2024) e03139, https://doi.org/10.1016/j.cscm.2024.e03139.

[46] G. Pagella, G. Ravenshorst, M. Mirra, W. Gard, J.-W. van de Kuilen, Innovative application of micro-drilling for the assessment of decay and remaining mechanical properties of historic wooden foundation piles in Amsterdam, Developments in the Built Environment 19 (2024) 100514, https://doi.org/10.1016/j.dibe.2024.100514.
[47] G. Pagella, M. Mirra, G. Ravenshorst, W. Gard, J.-W. van de Kuilen, Characterization of the remaining material and mechanical properties of historic wooden foundation piles in Amsterdam, Constr. Build. Mater. 450 (2024) 138616, https://doi.org/10.1016/j.conbuildmat.2024.138616.
[48] G. Pagella, M. Struik, M. Mirra, J.W. van de Kuilen, Small-scale testing of water-saturated wooden discs for determining the strength properties of timber foundation piles, Wood Mater. Sci. Eng. (2024) 1–3, https://doi.org/10.1080/17480272.2024.2426070.
[49] M.-J. Hemel, D.J. Peters, M. Korff, Bending properties and lateral resistance of historic timber foundation piles in Amsterdam, Netherlands, J. Struct. Eng. 151 (2025), https://doi.org/10.1061/JSENDH.STENG-13412.
[50] M. Korff, A. Venmans, P. Stoppelman, City scale InSAR monitoring of (buildings behind) quay walls, in: 2021 IEEE International Geoscience and Remote Sensing Symposium IGARSS, 2021, pp. 1966–1969, https://doi.org/10.1109/IGARSS47720.2021.9553784. IEEE.
[51] A.A.M. Venmans, M. op de Kelder, J. de Jong, M. Korff, M. Houtepen, Reliability of InSAR satellite monitoring of buildings near inner city quay walls, Proceedings of the International Association of Hydrological Sciences 382 (2020) 195–199, https://doi.org/10.5194/piahs-382-195-2020.
[52] D. Luongo, G. Nicodemo, A. Venmans, M. Korff, L. Sartorelli, H. Maljaars, D. Peduto, The quay walls of Amsterdam, Netherlands: an approach for collapse risk mitigation at the municipal scale based on multisource monitoring and surveying data, J. Geotech. Geoenviron. Eng. 151 (2025), https://doi.org/10.1061/JGGEFK.GTENG-12981.
[53] H. Kuai, V. Macchiarulo, S. Sharma, P. Karamitopoulos, F. Messali, G. Giardina, MT-InSAR optimisation for structural health monitoring, E-Journal of Nondestructive Testing 29 (2024), https://doi.org/10.58286/29753.
[54] R. van Dorst, R. Vervoorn, Non-invasive method for quay wall reconstruction in historic inner cities, in: International Conference on Soil Mechanics and Geotechnical Engineering, Seoul, South Korea, 2017.
[55] S. Sharma, M. Longo, F. Messali, Analysis procedures accounting for load redistribution mechanisms in masonry earth retaining structures under traffic loading, Eng. Struct. 315 (2024) 118420, https://doi.org/10.1016/j.engstruct.2024.118420.
[56] S. Sharma, M. Longo, F. Messali, A novel tier-based numerical analysis procedure for the structural assessment of masonry quay walls under traffic loads, Front Built Environ 9 (2023), https://doi.org/10.3389/fbuil.2023.1194658.
[57] X. Li, R. Esposito, A strategy for material characterisation of multi-wythe masonry Infrastructure: preliminary study, Constr. Build. Mater. 408 (2023) 133600, https://doi.org/10.1016/j.conbuildmat.2023.133600.
[58] Rijkswaterstaat. https://www.rijkswaterstaat.nl/en/water/water-management, 2023.
[59] B.V. Nebest, Marnixkade in Amsterdam. Funderingsonderzoek. Ref: 27854-01-01, Definitive, 2016. Vianen, the Netherlands.
[60] Rijkswaterstaat. https://www.rijkswaterstaat.nl/zakelijk/open-data/normaal-amsterdams-peil, 2023.
[61] R. Voortman, Personal Communication with Rick Voortman from Ingenieursbureau Gemeente Amsterdam, 2023.
[62] F. van Werkhoven, Personal Communication with Expert Mason F. Van Werkhoven, 2022.
[63] W. Voigt, Ueber die Beziehung zwischen den beiden Elasticitätsconstanten isotroper Körper, Ann. Phys. 274 (1889) 573–587, https://doi.org/10.1002/andp.18892741206.
[64] A. Reuss, Berechnung der Fließgrenze von Mischkristallen auf Grund der Plastizitätsbedingung für Einkristalle, ZAMM - Journal of Applied Mathematics and Mechanics/Z. Angew. Math. Mech. 9 (1929) 49–58, https://doi.org/10.1002/zamm.19290090104.
[65] N. Ramakrishnan, V.S. Arunachalam, Effective elastic moduli of porous solids, J. Mater. Sci. 25 (1990) 3930–3937, https://doi.org/10.1007/BF00582462.
[66] L. Grementieri, F. Daghia, L. Molari, G. Castellazzi, H. Derluyn, V. Cnudde, S. de Miranda, A multi-scale approach for the analysis of the mechanical effects of salt crystallisation in porous media, Int. J. Solid Struct. (2017) 225–239, https://doi.org/10.1016/j.ijsolstr.2017.08.009, 126–127.
[67] A.R. Boccaccini, Z. Fan, A new approach for the Young's modulus-porosity correlation of ceramic materials, Ceram. Int. 23 (1997) 239–245, https://doi.org/10.1016/S0272-8842(96)00033-8.